Universiteit
Antwerpen

This item is the archived peer-reviewed author-version of:

Secondary electron induced current in scanning transmission electron microscopy : an alternative way to visualize the morphology of nanoparticles

Reference:
Vlasov Evgenii, Skorikov Alexander, Sánchez-Iglesias Ana, Liz-Marzán Luis M., Verbeeck Johan, Bals Sara.- Secondary electron induced current in scanning transmission electron microscopy : an alternative way to visualize the morphology of nanoparticles
ACS materials letters / ACS - ISSN 2639-4979 - 5:7(2023), p. 1916-1921
Full text (Publisher's DOI): https://doi.org/10.1021/ACSMATERIALSLETT.3C00323
To cite this reference: https://hdl.handle.net/10067/1970040151162165141

uantwerpen.be
Institutional repository IRUA

Secondary electron induced current in scanning transmission electron microscopy: an alternative way to visualize the morphology of nano-particles

Evgenii Vlasov[1], Alexander Skorikov[1], Ana Sánchez-Iglesias[2,3], Luis Liz-Marzán[2,3,4,5], Johan Verbeeck[1], Sara Bals[1]*

[1] EMAT and NANOlab Center of Excellence, University of Antwerp, 2020 Antwerp, Belgium

[2] CIC biomaGUNE, Basque Research and Technology Alliance (BRTA), 20014 Donostia-San Sebastián, Spain

[3] Centro de Investigación Biomédica en Red, Bioingeniería, Biomateriales y Nanomedicina (CIBER-BBN), 20014 Donostia-San Sebastián, Spain

[4] Ikerbasque, Basque Foundation for Science, 48009 Bilbao, Spain

[5] CINBIO, University of Vigo, 36310 Vigo, Spain

ABSTRACT: Electron tomography (ET) is a powerful tool to determine the three-dimensional (3D) structure of nano-materials in a transmission electron microscope. However, the acquisition of a conventional tilt series for ET is a time-consuming process and can therefore not provide 3D structural information in a time-efficient manner. Here, we propose surface-sensitive secondary electron (SE) imaging as an alternative to ET for the investigation of the morphology of nano-materials. We use the SE electron beam induced current (SEEBIC) technique that maps the electrical current arising from holes, generated by the emission of SEs from the sample. We report that SEEBIC imaging may provide valuable information on the sample morphology with high spatial resolution and significantly shorter throughput times compared to ET. In addition, we discuss the contrast formation mechanisms to aid in the interpretation of SEEBIC data.

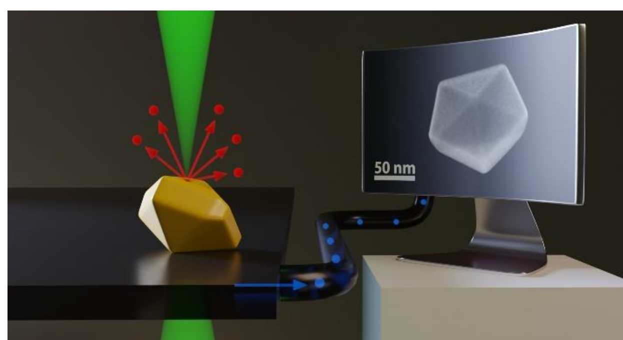

It is well known that the properties of nanomaterials are strongly connected to their size, shape, composition, and crystal structure.[1–3] Investigation of the local structure of nanomaterials is therefore of crucial importance to enable the optimization of a controlled synthesis as well as to tune the structure-property connection, leading to materials with specific, pre-defined properties. Electron microscopy has been a useful tool to perform such detailed characterization, at the level of individual nanoparticles. Although a plethora of electron microscopy imaging modes are available, a rough distinction can be made between Scanning Electron Microscopy (SEM) and Transmission Electron Microscopy (TEM). The difference between both approaches is related to the fact that in SEM mode one is predominantly probing the surface structure of a sample under investigation, whereas in TEM mode a projection of the entire sample is measured. SEM is quite user-friendly and often accessible in a scientific environment, but the resolution of a typical SEM instrument is of the order of 1-20 nm. On the other hand, (scanning) transmission electron microscopy ((S)TEM) yields (atomic resolution) information on both the structure and composition of a broad variety of nanomaterials, eventually along with signatures of their electronic and optical properties.[4] However, as already mentioned, TEM images conventionally only correspond to a two-dimensional (2D) projection of a three-dimensional (3D) object, which often hampers a clear understanding of the morphology of nanoparticles (NPs).

Electron tomography (ET) has therefore been developed as a technique to determine the 3D structure of nanomaterials from 2D images. These 2D projection images are acquired over a large tilt range and combined in a 3D reconstruction of the structure of interest through a mathematical algorithm.[5] During the past decades, ET in high-angle annular dark field STEM

(HAADF-STEM) mode has become a popular technique to investigate the overall morphology of nanomaterials, to determine the nature of surface facets, and even to characterize the atomic structure in 3D.[6–13] By applying ET in combination with techniques such as energy dispersive X-ray spectroscopy (EDXS)[14–16] or electron energy loss spectroscopy (EELS),[17–21] also the 3D investigation of composition and valence has become possible.[22] However, the acquisition of a conventional tilt series for ET is a time-consuming process that requires at least 1 hour for a standard experiment. In addition, after the acquisition, a post-process reconstruction step is required to evaluate the final 3D shape of the nanomaterial. Consequently, only a limited number of NPs can be investigated, hampering a general understanding of the average structure of a given sample. This restriction further limits a thorough understanding of the structure-property relations, especially because the properties of nanomaterials are mostly measured by ensemble techniques. It is therefore clear that ET is a very valuable technique, but still limited in providing 3D structural information in a time-efficient manner.

Bals and others recently developed methods to significantly accelerate the acquisition and reconstruction process for tomography.[23–25] On the other hand, it is interesting to note that, rather than obtaining a 3D reconstruction of the entire nanoparticle structure, the most important goal of many ET studies is often to only extract the surface morphology of the NPs. Indeed, the surface structure of a NP determines its reactivity, stability, and ability to interact with the environment. Especially the surface faceting of nanoparticles[26] is a key parameter toward modulating and optimizing the properties of metal/oxide NPs in catalytic,[27] plasmonic,[28,29] and medical[30] applications. Alternative characterization techniques that allow for high-resolution characterization of the surface structure without the need to acquire a full tilt series in ET would therefore enable a more time-efficient investigation, with better statistical value, for a broad range of samples. In this paper, we propose to investigate the surface structure of nanomaterials through the detection of secondary electrons (SEs) in STEM mode, while using the sample itself as the detector.

SEs are low-energy electrons (<50 eV) ejected from the sample during inelastic interactions with the primary electron beam. SEs originate from the near-surface region of the sample and therefore carry topographical information. The SE signal is therefore exploited in SEM as one of the main imaging modes.[31] However, typical field emission gun SEMs have SE imaging resolutions of just a few nm restricted by the size of the beam, the presence of aberrations, and signal delocalization due to electron-matter interactions.[31] These aspects limit the applicability of SEM for the investigation of nanoparticles with complex or irregular surface structures. Recently, SE detectors have been incorporated into a number of STEM instruments,[32] for which the higher acceleration voltages, compared to SEM, enabled SE images with resolutions down to the sub-nm regime.[33–36] It was demonstrated that SE imaging can complement conventional STEM modes, offering access to depth and topography information that is inaccessible by either phase contrast or (HA)ADF imaging.[37] With the development of aberration correctors, SE imaging with atomic resolution has been achieved[32,37–39] and SE imaging was furthermore combined with *in situ* heating to understand the behavior of supported catalysts during thermal treatments.[40] However, despite its demonstrated capabilities, SE imaging is not widely available in STEM.[32,37]

Recently, an alternative approach to detect SEs has been proposed,[41] based on a modification of the electron beam-induced current (EBIC) technique that has been widely used to analyze specific electrical properties of semiconductors.[42] EBIC conventionally measures the electrical current that originates when the primary electron beam interacts with the sample (e.g., generation of electron-hole pairs in a semiconductor device). In SE-related EBIC (SEEBIC), the detected current arises from holes generated by the emission of SEs from the sample.[41] Next, the current flows to a current-sensing transimpedance amplifier (TIA), and the detected signal will be equal but opposite to the generated SE current. The detected signal can be mapped pixel-by-pixel to produce an image that directly depends on the SE yield for each scan position.

The original paper by Hubbard *et al*.,[41] which introduced the technique, showed that SEEBIC is directly sensitive to the electronic properties of the materials, such as conductivity, connectivity, and work function. Later, it was demonstrated that lattice-resolution imaging is feasible,[43] as well as resistive contrast imaging allowing to visualize resistive grain boundaries in multilayer ceramic $BaTiO_3$ capacitors.[44] A series of papers by Dyck *et al.* have been issued, focusing on charge carrier transport in graphene nanodevices and the use of SEEBIC for device failure analysis.[45–47] SEEBIC allowed a clear distinction between single and multi-layer graphene, and visualization of cracks in graphene sheets.

So far, SEEBIC studies were primarily used to investigate the electronic properties of materials with a main emphasis on the importance of the technique for failure analysis and characterization of nanoelectronic devices. In this paper, we exploit another aspect of SEEBIC and discuss its use as an alternative technique to provide topographical information with high resolution. First, we will present experimental evidence that SEEBIC can overcome the lengthy acquisition and reconstruction procedures needed in ET, whereas the spatial resolution is superior to SEM imaging. Next, we will discuss the contrast formation mechanisms to aid in the interpretation of SEEBIC data.

Results and discussion

Au NPs can be synthesized with a broad variety of shapes and sizes.[26,48,49] Although the typical seeded-growth synthesis of such nanoparticles is well controlled, essential feedback about desirable NP shapes and features is often required, especially since the field has moved from highly symmetric to anisotropic, and more complex NPs. Here, we have studied Au NPs with different shapes: triangular platelets and Ino decahedra (Figure 1). An Ino decahedron contains 5 small lateral facets between the 10 facets of a perfect decahedron.[50] Conventional transmission electron micrographs, such as the HAADF-STEM images in Figure 1a,d, often fail to uniquely describe the shape and faceting of the NPs. ET allowed us to extract the necessary topographical information and clearly revealed the presence of side facets in triangular and decahedral NPs (Figure 1b,e), which is less obvious from the HAADF-STEM projections. However, the acquisition of the tilt series for ET took approximately 1 hour, which would hamper a high-throughput analysis.

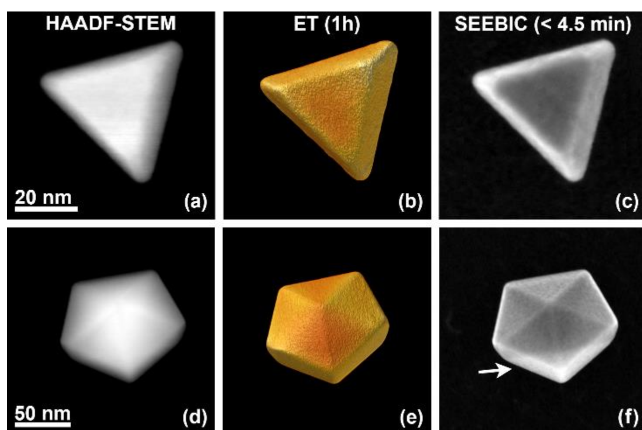

Figure 1. STEM images of an Au triangular platelet (a-c) and an Ino decahedron (d-e) obtained in different modes: (a, d) HAADF-STEM, (b, e) 3D surface visualization of an ET reconstruction, (c, f) SEEBIC imaging.

Next, SEEBIC was used to image the same particles (Figure 1c,f). The main concept of the SEEBIC setup is schematically shown in Figure 2. It is clear that both the morphology and the presence of side facets can be appreciated from the images. For the triangular platelet, a close-to-perfect agreement is found between the ET reconstruction and the SEEBIC image. However, for the Ino decahedron, subtle differences are present. For example, as indicated by a white arrow, a sharp line adjacent to an area with enhanced SEEBIC contrast is observed. To understand the origin of this contrast, we inspected the entire 3D structure as obtained by ET (see Figure S1). However, the apparent line and enhanced contrast cannot be discerned from the ET reconstruction, meaning that these features are of artifactual nature and are not related to any specific structural or compositional features in the NP. A further discussion of these observations will follow below. In addition, it should be noted that the method is not limited to metallic particles only, the main requirement for a SEEBIC experiment is the presence of a conductive underlying substrate from the sample to the amplifier (see Supporting Information and Figure S2).

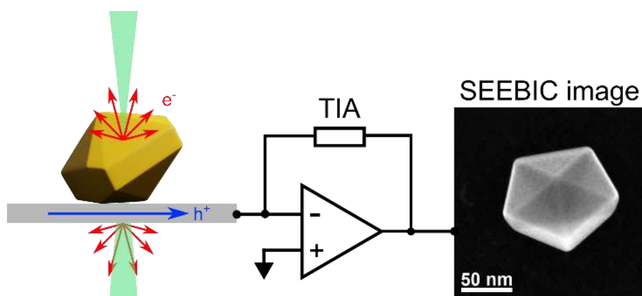

Figure 2. Schematic set-up of the SEEBIC imaging concept. Red arrows indicate directions of SE emission form the surfaces of NP, blue arrow – net hole current flowing into TIA input.

By comparing the electron dose accumulated during both ET and SEEBIC experiments presented in Figure 1 (see Supporting Information for details) we concluded that using our current setup, SEEBIC is one order of magnitude less dose-efficient compared to conventional ET. On the other hand, the acquisition time for a single 512×512 SEEBIC image in Figure 1c and f was 4.5 min (dwell time of 1ms), which means a drastic reduction in the acquisition time (up to 13 times in this case).

Further optimization of the experimental parameters (high voltage and dwell time) demonstrates that both dose and acquisition time can be significantly reduced while preserving the signal-to-noise ratio at level that still enables a clear interpretation of the particle morphology. Figure 3 shows that acquisition times of approximately half a minute per image as feasible. Overall, this results in a time reduction of two orders of magnitude in comparison to the acquisition for ET. The electron dose can also be further reduced, rendering SEEBIC equally or even more dose efficient as ET. Consequently, SEEBIC will enable to improve the throughput of 3D characterization as well as to investigate nanoparticle transformations during the *in situ* application of specific triggers such as e.g. heat.

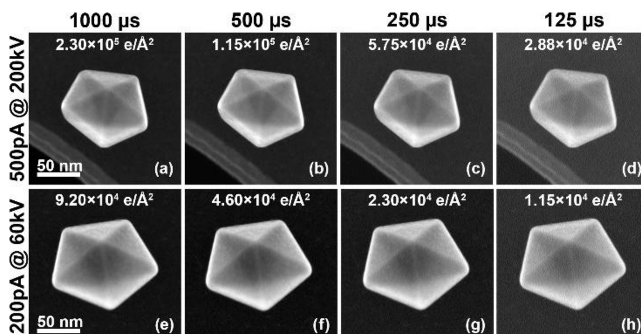

Figure 3. SEEBIC images of Au Ino decahedra obtained at various experimental conditions and dwell times. The accumulated dose is indicated in each panel.

Next, we compare SEEBIC imaging with conventional SEM images (Figure 4). Because of (unavoidable) different experimental conditions, a direct comparison is not straightforward. Nevertheless, it is clear that the SEEBIC yields superior image quality. To estimate the image resolution obtained by SEM and SEEBIC, we used the edge spread function (ESF), based on intensity profiles acquired across the edges of the nanoparticles, as indicated by white arrows in Figure S3. The ESF is a result of a convolution of a sharp edge of the NPs with a point spread function (PSF) that is directly connected to spatial resolution. If we assume a PSF that is described by the logistic distribution curve, we obtain a sigmoid function for the ESF.[51]

$$ESF(x) = \frac{a}{1 + \exp\left(\frac{r - x}{\sigma}\right)} + b$$

In this expression, *a* and *b* correspond to scaling factors and *r* is the position of the edge. The parameter σ is related to the full width at half maximum $\mathrm{FWHM} = 2\ln\left(3 + \sqrt{8}\right)\sigma = 3.53\sigma$,[52] which we here consider as an estimate for the spatial resolution. In this manner, we estimate the spatial resolution of the SEM images as approx. 4.2 nm, while the nominal resolution of the instrument was listed as 0.8 nm (see Supporting Information). The discrepancy between actual and nominal spatial resolution can be explained in terms of spatial beam broadening due to electron scattering in the material and the support.[53] The SEEBIC images yield a clearly higher spatial resolution, estimated to be 1.3 nm. The SEEBIC resolution is limited by the selected sampling, which was balanced between a sufficient field of view and the total acquisition time. It should be noted,

however, that the theoretical resolution is governed by the obtainable probe size. The improvement of spatial resolution using SEEBIC in comparison to SEM is especially important when imaging NPs with sizes smaller than 50 nm (Figure 4a-b). We used a similar approach to estimate the spatial resolution of obtained ET data.[51] Note that the resolution of ET data has anisotropic nature due to the geometry of the experiment. The obtained resolution values are 0.77 nm for the x-axis, 0.76 nm for the y-axis, and 0.98 nm for the z-axis (Figure S4).

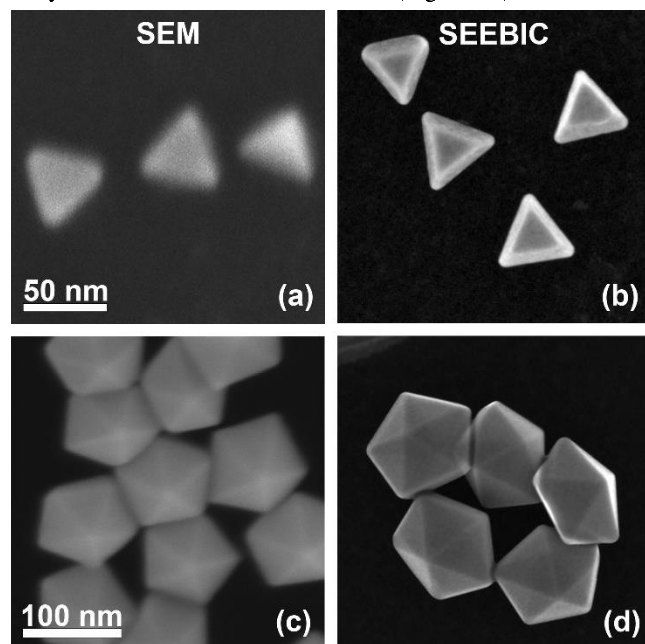

Figure 4. Conventional SEM (a, c) and SEEBIC images (b, d) of Au triangles (a, b) and Au Ino decahedra (c, d) showing qualitatively similar images, even though the detection scheme is very different. Note how SEEBIC provides a significantly higher spatial resolution revealing details of the sample that are not visible in SEM imaging.

SEEBIC topography contrast mechanisms

As demonstrated above, SEEBIC images show a close resemblance to SEM images, which is not surprising given that they are both formed through the creation of SEs. However, the white arrow in Figure 1f illustrates the presence of artifactual features that cannot be understood in terms of surface contrast. For SEEBIC to become a useful alternative for ET, it is important to understand the origin of these artifacts.

In a SEM experiment, the acceleration voltage is lower in comparison to typical (S)TEM and consequently, SEs are predominantly generated at the top surface of the nanoparticles.[54] In the case of (S)TEM, however, the incident electron beam traverses the sample and SEs are emitted from both the top and bottom surfaces. Because of the strong magnetic field (~2T) in the pole-piece gap of the TEM, the SEs that leave the nanoparticle during a SEEBIC experiment will either spiral up or down. For the electrons spiraling up, the generated SEs leave the nanoparticles in a charged state and to reestablish the charge balance, the holes corresponding to emitted SEs flow to the transimpedance amplifier, which will generate the topographical contrast observed in SEEBIC images. On the other hand, the electrons that spiral down might be re-absorbed by structural features along their trajectories. Due to their extremely short inelastic mean free path (approx. 1-2 nm for C),[55] these low-energy SEs are readily absorbed by the TEM support, corresponding to, e.g., a few nm-thick amorphous carbon layer. In this manner, the EBIC current that would otherwise flow to the amplifier is compensated, resulting in a contrast that is dominated by the top surface of the nanoparticles.

Oppositely, when a nanoparticle is partially suspended over a hole in the support film, which is the case for the particle in Figure 5a-c, a significant portion of SEs generated at the bottom surface can escape without being absorbed and consequently contribute to the SEEBIC image formation. As a result, an image is formed that contains contributions of both the front and back surfaces, as indicated by the white arrows in Figure 5c. Even if the particle is lying on a closed membrane support (continuous conductive film), non-topographical contrast might be present, which is exemplified by the sharp line in Figures 1f and 5f. In this case, the Au Ino decahedron lies on one of its facets, resulting in a gap between the other NP facets and the support film, as schematically illustrated in Figure 5d and Figure S5. Consequently, a fraction of the SEs emitted from the bottom facets escapes without being re-captured by the support film (Figure 5d, red arrows). This fraction is determined by the angle-dependent scattering cross-section for SEs and the orientation of the NP's surface normal relative to the magnetic field axis. The apparent line in SEEBIC consequently corresponds to the edges of the Ino decahedron that form the boundary between the 'base' of a NP and its suspended part, leading to abrupt changes in contrast. It should be noted that this line is also present in HAADF-STEM because of local changes in sample thickness due to the presence of the edges of Ino decahedron (Figure S5). The described effect can be used for understanding artifactual features arising in Figure 4d (see Supporting information for more details).

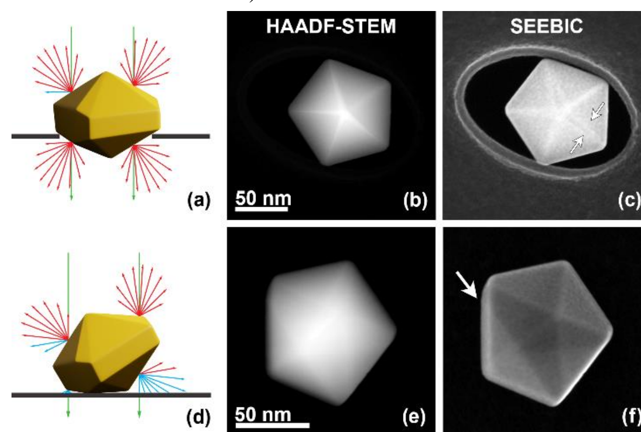

Figure 5. (a, d) 3D visualization of the NPs on the support film. (b, e) HAADF-STEM and (c, f) SEEBIC images of Au decahedra. Red arrows indicate SEs escaping the surface of NPs without being absorbed by the support, and blue arrows indicate re-captured SEs. The lengths of the arrows on panels (a) and (d) are indicative of the number of SEs emitted in each direction and proportional to the cosine of the angle between this direction and the surface normal. Green arrows indicate primary electron beam.

Conclusions

In conclusion, we have demonstrated that SEEBIC can be considered as an attractive approach to image the morphology of nanomaterials with shorter acquisition and processing times in comparison to ET and superior resolution in comparison to SEM. We discussed the importance of using a closed membrane to avoid minimize imaging artifacts. Direct access to surface morphology obtainable in the order of minutes opens up the possibility to use SEEBIC for high-throughput analysis and combine 3D imaging with *in situ* stimuli. Future work will focus on further increasing the signal-to-noise ratio and/or reducing the frame times.

ASSOCIATED CONTENT

Supporting Information. Supporting information includes additional images, experimental details, and synthesis details (PDF). Supporting movies used for inspection of particle morphology (MP4). This material is available free of charge via the Internet at http://pubs.acs.org.

AUTHOR INFORMATION

Corresponding Author

*E-mail: Sara.Bals@uantwerpen.be.

Author Contributions

The manuscript was written through contributions of all authors. All authors have given approval to the final version of the manuscript.

ACKNOWLEDGMENT

The funding for this project was provided by European Research Council (ERC Consolidator Grant 815128, REALNANO). JV acknowledges the eBEAM project which is supported by the European Union's Horizon 2020 research and innovation program under grant agreement No 101017720 (FET-Proactive EBEAM). L.M.L.-M. acknowledges funding from MCIN/AEI/10.13039/501100011033 (Grant # PID2020-117779RB-I00).

REFERENCES

(1) El-Sayed, M. A. Some Interesting Properties of Metals Confined in Time and Nanometer Space of Different Shapes. *Acc. Chem. Res.* **2001**, *34*, 257–264.

(2) Daniel, M.-C.; Astruc, D. Gold Nanoparticles: Assembly, Supramolecular Chemistry, Quantum-Size-Related Properties, and Applications toward Biology, Catalysis, and Nanotechnology. *Chem. Rev.* **2004**, 104, 293–346.

(3) Hornyak, G. L.; Tibbals, H. F.; Dutta, J.; Moore, J. J. *Introduction to Nanoscience and Nanotechnology;* CRC Press, 2008.

(4) Van Tendeloo, G.; Bals, S.; Van Aert, S; Verbeeck, J.; Van Dyck, D. Advanced Electron Microscopy for Advanced Materials. *Adv. Mater.* **2012**, *24*, 5655–5675.

(5) Van Aarle, W.; Palenstijn, W. J.; De Beenhouwer, J.; Altantzis, T.; Bals, S.; Batenburg, K. J.; Sijbers, J. The ASTRA Toolbox: A Platform for Advanced Algorithm Development in Electron Tomography. *Ultramicroscopy* **2015**, *157*, 35–47.

(6) Midgley, P. A.; Weyland, M.; Meurig Thomas, J.; Johnson, B. F. G. Z-Contrast tomography: a technique in three-dimensional nanostructural analysis based on Rutherford scattering. *Chem. Commun.* **2001**, 10, 907–908.

(7) Midgley, P. A.; Weyland, M. 3D Electron Microscopy in the Physical Sciences: The Development of Z-Contrast and EFTEM Tomography. *Ultramicroscopy* **2003**, *96*, 413–431.

(8) Bals, S.; Van Tendeloo, G.; Kisielowski, C. A New Approach for Electron Tomography: Annular Dark-Field Transmission Electron Microscopy. *Adv. Mater.* **2006**, *18*, 892–895.

(9) Midgley, P. A.; Dunin-Borkowski, R. E. Electron Tomography and Holography in Materials Science. *Nat. Mater.* **2009**, *8*, 271–280.

(10) Bals, S.; Casavola, M.; Van Huis, M. A.; Van Aert, S.; Batenburg, K. J.; Van Tendeloo, G.; Vanmaekelbergh, D. Three-Dimensional Atomic Imaging of Colloidal Core-Shell Nanocrystals. *Nano. Lett.* **2011**, *11*, 3420–3424.

(11) Goris, B.; Bals, S.; Van den Broek, W.; Carbó-Argibay, E.; Gómez-Graña, S.; Liz-Marzán, L. M.; Van Tendeloo, G. Atomic-Scale Determination of Surface Facets in Gold Nanorods. *Nat. Mater.* **2012**, *11*, 930–935.

(12) Bals, S.; Goris, B.; Liz-Marzán, L. M.; Van Tendeloo, G. Three-Dimensional Characterization of Noble-Metal Nanoparticles and Their Assemblies by Electron Tomography. *Angew. Chem. Int. Ed.* **2014**, *53*, 10600-10610.

(13) Miao, J.; Ercius, P.; Billinge, S. J. L. Atomic Electron Tomography: 3D Structures without Crystals. *Science* **2016**, *353*, aaf2157-1-9.

(14) Goris, B.; Polavarapu, L.; Bals, S.; Van Tendeloo, G.; Liz-Marzán, L. M. Monitoring Galvanic Replacement through Three-Dimensional Morphological and Chemical Mapping. *Nano. Lett.* **2014**, *14*, 3220–3226.

(15) Polavarapu, L.; Zanaga, D.; Altantzis, T.; Rodal-Cedeira, S.; Pastoriza-Santos, I.; Pérez-Juste, J.; Bals, S.; Liz-Marzán, L. M. Galvanic Replacement Coupled to Seeded Growth as a Route for Shape-Controlled Synthesis of Plasmonic Nanorattles. *J. Am. Chem. Soc.* **2016**, *138*, 11453–11456.

(16) Zanaga, D.; Altantzis, T.; Bals, S.; Polavarapu, L.; Liz-Marzán, L. M.; Freitag, B.; Zanaga, D.; Altantzis, T.; Polavarapu, L.; Liz-Marzán, L. M.; Freitag, B.; Bals, S. A New Method for Quantitative XEDS Tomography of Complex Heteronanostructures. *Part. Part. Syst. Charact.* **2016**, *33*, 396–403.

(17) Nicoletti, O.; de La Peña, F.; Leary, R. K.; Holland, D. J.; Ducati, C.; Midgley, P. A. Three-Dimensional Imaging of Localized Surface Plasmon Resonances of Metal Nanoparticles. *Nature* **2013**, *502*, 80–84.

(18) Goris, B.; Turner, S.; Bals, S.; Van Tendeloo, G. Three-Dimensional Valency Mapping in Ceria Nanocrystals. *ACS Nano* **2014**, *8*, 10878–10884.

(19) Goris, B.; Meledina, M.; Turner, S.; Zhong, Z.; Batenburg, K. J.; Bals, S. Three Dimensional Mapping of Fe Dopants in Ceria Nanocrystals Using Direct Spectroscopic Electron Tomography. *Ultramicroscopy* **2016**, *171*, 55–62.

(20) Torruella, P.; Arenal, R.; de La Peña, F.; Saghi, Z.; Yedra, L.; Eljarrat, A.; López-Conesa, L.; Estrader, M.; López-Ortega, A.; Salazar-Alvarez, G.; *et al*. 3D Visualization of the Iron Oxidation State in FeO/Fe3O4 Core-Shell Nanocubes from Electron Energy Loss Tomography. *Nano Lett.* **2016**, *16*, 5068–5073.

(21) Haberfehlner, G.; Schmidt, F. P.; Schaffernak, G.; Hörl, A.; Trügler, A.; Hohenau, A.; Hofer, F.; Krenn, J. R.; Hohenester, U.; Kothleitner, G. 3D Imaging of Gap Plasmons in Vertically Coupled Nanoparticles by EELS Tomography. *Nano Lett.* **2017**, *17*, 6773–6777.

(22) Jenkinson, K.; Liz-Marzán, L. M.; Bals, S. Multimode Electron Tomography Sheds Light on Synthesis, Structure, and Properties of Complex Metal-Based Nanoparticles. *Adv. Mater.* **2022**, *34*, 2110394-1-19.

(23) Vanrompay, H.; Bladt, E.; Albrecht, W.; Béché, A.; Zakhozheva, M.; Sánchez-Iglesias, A.; Liz-Marzán, L. M.; Bals, S. 3D Characterization of Heat-Induced Morphological Changes of Au Nanostars by Fast in Situ Electron Tomography. *Nanoscale* **2018**, *10*, 22792–22801.

(24) Vanrompay, H.; Skorikov, A.; Bladt, E.; Béché, A.; Freitag, B.; Verbeeck, J.; Bals, S. Fast versus Conventional HAADF-STEM Tomography of Nanoparticles: Advantages and Challenges. *Ultramicroscopy* **2021**, *221*, 113191-1-10.
(25) Albrecht, W.; Bals, S. Fast Electron Tomography for Nanomaterials. *J. Phys. Chem. C* **2020**, *124*, 27276–27286.
(26) Niu, W.; Xu, G. Crystallographic Control of Noble Metal Nanocrystals. *Nano Today* **2011**, *6*, 265–285.
(27) Li, Y.; Somorjai, G. A. Nanoscale Advances in Catalysis and Energy Applications. *Nano Lett.* **2010**, *10*, 2289–2295.
(28) Sepúlveda, B.; Angelomé, P. C.; Lechuga, L. M.; Liz-Marzán, L. M. LSPR-Based Nanobiosensors. *Nano Today* **2009**, *4*, 244–251.
(29) Atwater, H. A.; Polman, A. Plasmonics for Improved Photovoltaic Devices. *Nat. Mater.* **2010**, *9*, 205–213.
(30) Jain, P. K.; El-Sayed, I. H.; El-Sayed, M. A. Au Nanoparticles Target Cancer. *Nano Today* **2007**, *2*, 18–29.
(31) Goldstein, J. I.; Newbury, D. E.; Michael, J. R.; Ritchie, N. W. M.; Scott, J. H. J.; Joy, D. C. *Microscopy and X-Ray Microanalysis*; Springer, 2018.
(32) Inada, H.; Zhu, Y. Secondary Electron Microscopy in STEM. In *Scanning Transmission Electron Microscopy of Nanomaterials: Basics of Imaging and Analysis* **2014**, 307–344.
(33) Allen, R. M. Secondary Electron Imaging as an Aid to STEM Microanalysis. *Ultramicroscopy* **1982**, *10*, 237–245.
(34) Hembree, G. G.; Crozier, P. A.; Drucker, J. S.; Krishnamurthy, M.; Venables, J. A.; Cowley, J. M. Biased Secondary Electron Imaging in a UHV-STEM. *Ultramicroscopy* **1989**, *31*, 111–115.
(35) Liu, J.; Cowley, J. M. Imaging with High-Angle Scattered Electrons and Secondary Electrons in the STEM. *Ultramicroscopy* **1991**, *37*, 50–71.
(36) Howie, A. Recent Developments in Secondary Electron Imaging. *J. Microsc.* **1995**, *180*, 192–203.
(37) Mitchell, D. R. G.; Casillas, G. Secondary Electron Imaging in an Aberration-Corrected STEM. *Micros. Today* **2016**, *24*, 22–27.
(38) Ciston, J.; Brown, H. G.; D'Alfonso, A. J.; Koirala, P.; Ophus, C.; Lin, Y.; Suzuki, Y.; Inada, H.; Zhu, Y.; Allen, L. J.; *et al.* Surface Determination through Atomically Resolved Secondary-Electron Imaging. *Nat. Commun.* **2015**, *6*, 1–8.
(39) Zhu, Y.; Inada, H.; Nakamura, K.; Wall, J. Imaging Single Atoms Using Secondary Electrons with an Aberration-Corrected Electron Microscope. *Nat. Mater.* **2009**, *8*, 808–812.
(40) Howe, J. Y.; Allard, L. F.; Bigelow, W. C.; Demers, H.; Overbury, S. H. Understanding Catalyst Behavior during in Situ Heating through Simultaneous Secondary and Transmitted Electron Imaging. *Nanoscale Res. Lett.* **2014**, *9*, 1-6.
(41) Hubbard, W. A.; Mecklenburg, M.; Chan, H. L.; Regan, B. C. STEM Imaging with Beam-Induced Hole and Secondary Electron Currents. *Phys. Rev. Appl.* **2018**, *10*, 044066-1-7.
(42) Everhart, T. E.; Wells, O. C.; Matta, R. K. A Novel Method of Semiconductor Device Measurements. *Proceedings of the IEEE* **1964**, *52*, 1642–1647.
(43) Mecklenburg, M.; Hubbard, W. A.; Lodico, J. J.; Regan, B. C. Electron Beam-Induced Current Imaging with Two-Angstrom Resolution. *Ultramicroscopy* **2019**, *207*, 112852-1-5.
(44) Hubbard, W. A.; Lingley, Z.; Theiss, J.; Sitzman, S.; Ayvazian, T.; Brodie, M.; Foran, B. Scanning Transmission Electron Microscope Mapping of Electronic Transport in Polycrystalline BaTiO3 Ceramic Capacitors. *Appl. Phys. Lett.* **2019**, *115*, 133502-1-5.
(45) Dyck, O.; Swett, J. L.; Lupini, A. R.; Mol, J. A.; Jesse, S. Imaging Secondary Electron Emission from a Single Atomic Layer. *Small Methods* **2021**, *5*, 2000950-1-7.
(46) Dyck, O.; Swett, J. L.; Evangeli, C.; Lupini, A. R.; Mol, J. A.; Jesse, S. Mapping Conductance and Switching Behavior of Graphene Devices In Situ. *Small Methods* **2022**, *6*, 2101245-1-7.
(47) Dyck, O.; Swett, J. L.; Evangeli, C.; Lupini, A. R.; Mol, J.; Jesse, S. Contrast Mechanisms in Secondary Electron E-Beam-Induced Current (SEEBIC) Imaging. *Microsc. Microanal.* **2022**, *28*, 1567–1583.
(48) Grzelczak, M.; Pérez-Juste, J.; Mulvaney, P.; Liz-Marzán, L. M. Shape Control in Gold Nanoparticle Synthesis. *Chem. Soc. Rev.* **2008**, *37*, 1783–1791.
(49) Tao, A. R.; Habas, S.; Yang, P. Shape Control of Colloidal Metal Nanocrystals. *Small* **2008**, *4*, 310–325.
(50) Ino, S. Stability of Multiply-Twinned Particles. *J. Phys. Soc. Jpn.* **1969**, *27*, 941–953.
(51) Heidari Mezerji, H.; Van den Broek, W.; Bals, S. A Practical Method to Determine the Effective Resolution in Incoherent Experimental Electron Tomography. *Ultramicroscopy* **2011**, *111*, 330-336.
(52) Aschwanden, M. Analytical SOC Models. In *Self-Organized Criticality in Astrophysics* **2011**, 83–110.
(53) Reimer, L. Scanning Electron Microscopy; Springer, *2008*.
(54) Lin, Y.; Joy, D. C. A New Examination of Secondary Electron Yield Data. *Surf. Interface Anal.* **2005**, *37*, 895–900.
(55) Ziaja, B.; van der Spoel, D.; Szöke, A.; Hajdu, J. Auger-Electron Cascades in Diamond and Amorphous Carbon. *Phys. Rev. B* **2001**, *64*, 214104-1-8.

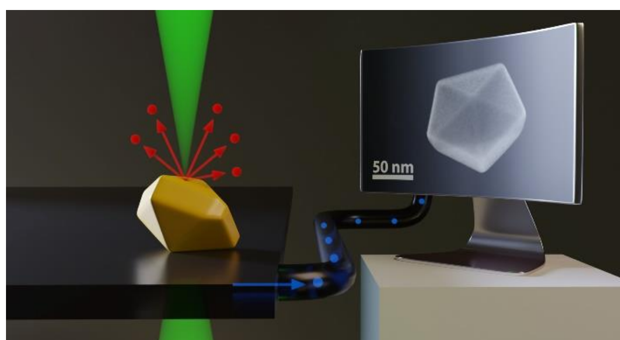

For Table of Contents Only